J Membrane Biol (2015) 248:979–990
DOI 10.1007/s00232-015-9809-6

Large Deformation Properties of Red Blood Cell Membrane Based on a Higher Order Gradient Quasi-continuum Model

X. Y. Wang[1] · J. B. Wang[2] · B. B. Qiu[3] · L. F. Hu[1]

Received: 18 March 2015 / Accepted: 5 May 2015 / Published online: 14 May 2015

Abstract Based on the proposed higher order gradient quasi-continuum model, the numerical investigations of the basic mechanical properties and deformation behaviors of human red blood cell (RBC) membrane under large deformation at room temperature (i.e., 300 K) are carried out in the present paper. The results show that RBC membrane is a nonlinear hyperelastic material. The mechanical properties of RBC membrane is dominated by isotropic nature at the stage of initial deformation, however, its anisotropic material properties emerge clearly with the loading increasing. The out-of-plane wrinkling of RBC membrane upon shear loading can be reproduced numerically. With the use of the so-called higher order Cauchy–Born rule as the kinematic description, the bending stiffness of RBC membrane can be considered conveniently.

Keywords Red blood cell membrane · Spectrin network · Higher order Cauchy–Born rule · Quasi-continuum model · Meshless method

✉ X. Y. Wang
wxy017@126.com

[1] School of Transportation, Ludong University, Yantai, Shandong 264025, China

[2] School of Shipping and Ports Architecture Engineering, Zhejiang Ocean University, Zhoushan, Zhejiang 316022, China

[3] Sheng'an Construction Group Co. Ltd, Zibo, Shandong 255000, China

Introduction

As the main component of human red blood cells (RBCs), which are often used as models for investigating the fundamental properties of complex nucleated cells, RBC membrane has attracted more attention in the past years. It has been confirmed that many hemolytic anemia disorders such as sickle cell anemia are in close associated with the deformation characteristics and mechanical properties of RBC membrane (An and Mohandas 2008; Bratosin et al. 2011; Delaunaya 2004). Therefore, it is very imperative and important to have a thorough knowledge of the memchanical properties and deformation behaviors of RBC.

For the mechanical properties of RBC membrane and RBCs, many continuum mechanics models have been developed. Hansen et al. (1996) established a continuum model for predicting the elastic shear modulus and the area expansion modulus of RBC membrane skeleton with use of elastic springs to describe the spectrin molecules. In this model, the authors applied the treatment of the random Delaunay triangulation to organize the topology of the planar spectrin network patch. Boey et al. (1998) studied the in-plane compression modulus and shear modulus of RBC spectrin network in the context of continuum framework with use of three structural models, i.e., the stress-free model, the prestress model, and the condensed model. In their work, the cytoskeletal network is equivalent to a low-temperature Hookean spring system. Subsequently, they developed a coarse-grained molecular model for predicting the mechanical properties of erythrocyte membrane with involving the two- and three-body effective potentials in the resulting energy formulation to overcome the drawbacks of their spring models (Discher et al. 1998). Lenormand et al. (2001) considered the RBC

membrane skeleton network as a continuous, homogeneous, and isotropic elastic medium to measure its area expansion and shear moduli. Mukhopadhyay et al. (2002) proposed a continuum mechanical model to investigate the shapes of RBC and the mechanical properties of RBC membrane skeleton. Dao et al. (2003) and Mills et al. (2004) extracted mechanical properties of RBC membrane in the context of continuum mechanics with use of the one-parameter Neo-Hookean form and the two-parameter Yeoh form, respectively, to construct the corresponding constitutive models.

There are also many worm-like-chain (WLC)-based coarse-grained, or mesoscopic, models have been developed for simulating RBC membrane and RBCs. The advantages of coarse-grained models are that the phenomena of RBC membrane can be investigated in detail without any parameter fitting and the computation efforts can be saved largely. Based on the free energy theory, Dao et al. (2006) proposed a molecularly based multiscale model for RBC membrane to predict its several in-plane mechanical parameters. The shear modulus, the linear area compression modulus, and the Young's modulus of RBC membrane obtained are consistent with the results from the neo-Hookean-based hyperelastic models. In the context of dissipative particle dynamics, Fedosov et al. (2010) presented a multiscale mesoscopic model for RBCs where the RBC membrane is described with WLC model. With the use of this multiscale model, they studied the motion of RBC membrane. Hartmann (2010) developed a continuum multiscale model for mechanics of RBC based on the theory of Γ-convergence considering the RBC membrane as a two-dimensional hypersurface. With the use of the so-called higher order Cauchy–Born rule (HCB rule), Wang et al. (2014) proposed a nanoscale quasi-continuum (QC) model for exploring the mechanical properties and large deformation behaviors of RBCs. As the second-order deformation gradient tensor involving in the constitutive model, the curvature effect of RBC membrane can be taken into account naturally.

However, to the best of the authors' knowledge, there are few works devoted to the investigation of mechanical properties of RBC membrane at large deformation. In the present paper, we attempt to use the established higher order gradient QC model and meshless numerical computational scheme, of which the HCB rule is utilized to construct the constitutive model, for the investigation of large deformation properties of RBC membrane at room temperature. From the statistical physics point of view, RBC membrane can be treated as an equivalent 2-dimensional supersurface with no thickness. The representative cell of the spectrin network underlying in the equivalent initial/unstressed RBC membrane is assumed with hexagonal symmetry and its topological structure is presumed to be unchanged during deformation. The advantages of the proposed method: (1) The information of the microscopic structure of RBC membrane skeleton network can be incorporated into the equivalent continuum membrane; (2) the computational efforts can be saved greatly since the number of degrees of freedom involving large molecular systems can be chosen freely; and (3) the bending stiffness of RBC membrane, which is corresponding to the curvature effect of the membrane, can be captured in a geometrically consistent way with the use of HCB rule as the kinematic description.

The plan of the paper is as follows. In "Model of Red Blood Cell Membrane" section, the model of RBC membrane based on the WLC is introduced. "Constitutive Model for RBC Membrane" section is devoted to formulate the hyperelastic constitutive model for RBC membrane with use of HCB rule as the kinematic description. Based on the proposed constitutive relationship, several in-plane mechanical properties of RBC membrane under large deformation at room temperature are investigated in "The In-Plane Elastic Properties of RBC Membrane" section. "Meshless Numerical Computational Scheme" section aims at the construction of the meshless numerical simulation scheme for the large deformation of RBC membrane sheets. "Numerical Examples and Discussion" section gives several numerical examples and discussion for RBC membrane fragments under large deformation at 300 K. Finally, some concluding remarks are given in "Concluding Remarks" section.

Model of Red Blood Cell Membrane

As known to all, human RBC membrane has two main components: the underlying spectrin network/membrane skeleton and the phospholipid bilayer which adheres on the spectrin network. The total Helmholtz free energy of RBC membrane under large deformation such as under tension or shear deformation is mainly supplied by the in-plane energy from spectrin network and lipid bilayer (Dao et al. 2006). The bending energy stored in lipid bilayer, which is much smaller than the in-plane energy especially at large tension/shear deformation, is neglected in the present study. The representative cell of the undeformed spectrin network is assumed to be a symmetrical hexagon, considering the fact that the topological structure of the spectrin network is primarily constructed by hexagonal lattices (Liu et al. 1987). All the spectrin filaments in the representative cell have same original length (see Fig. 1 for reference). The RBC membrane is equivalent to be a 2D surface without thickness and the topological structure of the spectrin network is presumed unchanged during deformation. Based on the preparation made above, the total

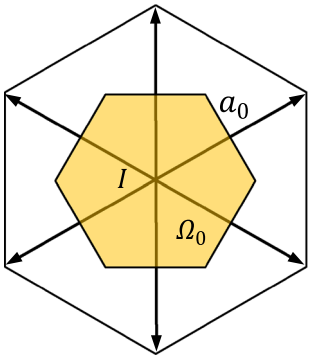

Fig. 1 The representative cell corresponding to junction I

Helmholtz free energy density of a representative cell can be expressed as

$$W_T(\boldsymbol{F},\boldsymbol{G}) = \frac{\left(\frac{1}{2}\sum_{J=1}^{6} U_{\mathrm{WLC}}(|\boldsymbol{r}_{IJ}|) + \frac{1}{3}\sum_{\gamma=1}^{6} U_{\mathrm{S}}(A_\gamma)\right)}{\Omega_0}, \tag{1}$$

where $\Omega_0 = \sqrt{3}a_0^2/2$ denotes the area of a representative cell in which a_0 is the length of the spectrin filament (see Fig. 1 for reference). $|\boldsymbol{r}_{IJ}|(J = 1,\ldots,6)$ denotes the length of the lattice vector $\boldsymbol{r}_{IJ}$ between the junction points I and J. As mentioned by Arroyo and Belytschko (2002), it is impossible to correctly describe the curvature effect of a hyperelastic membrane, which is corresponding to the bending stiffness, with the only use of the first-order linear kinematic relationship. Therefore, the standard Cauchy–Born rule (CB rule), in which only the first-order deformation gradient tensor included, is not suitable for the kinematic description of RBC membrane. Fortunately, the curvature effect of a two-dimensional manifold can be captured conveniently through the so-called higher order Cauchy–Born rule (HCB rule) proposed by Guo et al. (2006) due to involving the second-order deformation gradient tensor. Consequently, based on HCB rule as the kinematic description (see Fig. 2 for an illustration), the lattice vector $\boldsymbol{r}_{IJ}$ can be given as

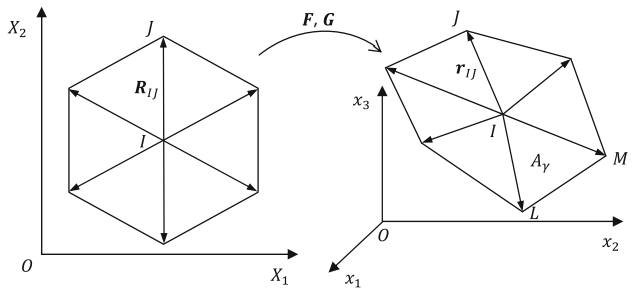

Fig. 2 Illustration of the so-called higher order Cauchy–Born rule

$$\boldsymbol{r}_{IJ} = \boldsymbol{F}\cdot\boldsymbol{R}_{IJ} + \frac{1}{2}\boldsymbol{G} : (\boldsymbol{R}_{IJ}\otimes\boldsymbol{R}_{IJ}), \tag{2}$$

with $\boldsymbol{F}$ and $\boldsymbol{G}$ denoting the first- and second-order deformation gradient tensor, respectively. $\boldsymbol{R}_{IJ}$ is the lattice vector between junction points I and J in the reference/initial configuration. The area $A_\gamma(\gamma = 1,\ldots,6)$ in Eq. (1) between $\boldsymbol{r}_{IL}$ and $\boldsymbol{r}_{IM}$ can be calculated by (see Fig. 2 for reference)

$$A_\gamma = \frac{1}{2}|\boldsymbol{r}_{IL}\times\boldsymbol{r}_{IM}| = \frac{1}{2}|\boldsymbol{r}_{IL}||\boldsymbol{r}_{IM}|\sin(\boldsymbol{r}_{IL},\boldsymbol{r}_{IM}), \tag{3}$$

where the subscripts I, L, and M denote different junction points and are not implied summation.

In Eq. (1), the entropic free energy U_{WLC} stored in spectrin links can be expressed in terms of the two-body potential for DNA, i.e., the so-called WLC model (Marko and Siggia 1995)

$$U_{\mathrm{WLC}}(a) = \frac{k_{\mathrm{B}}T}{4pa_{\max}}\cdot\frac{a^2(3a_{\max}-2a)}{a_{\max}-a}, \tag{4}$$

in which a denotes the chain length and $a_{\max}$ is maximum/contour length of the chain. p represents the persistence length. $k_{\mathrm{B}} = 1.38\times10^{-23}\,\mathrm{J\ K^{-1}}$ is the Boltzmann constant. T is the absolute temperature.

The elastic potential U_{S} in Eq. (1) stored in the lipid bilayer membrane can be calculated in the following form

$$U_{\mathrm{S}}(A_\gamma) = \frac{C}{A_\gamma^q}, \tag{5}$$

where the parameter q can be chosen freely for different models. In the present paper, q is selected as 1. The value of the constant C can be obtained under the condition that RBC membrane is initially unstressed (refer to Wang et al. (2014) for more details).

Constitutive Model for RBC Membrane

Based on the established regular hexagonal RBC membrane network, the formulation of its hyperelastic constitutive model is presented in the present section. Combining with the free energy density of the representative cell given in Eq. (1), the first Piola–Kirchhoff stress tensor $\boldsymbol{P}$ and the higher order stress tensor $\boldsymbol{Q}$, which are work conjugate to $\boldsymbol{F}$ and $\boldsymbol{G}$, respectively, can be derived from

$$\begin{aligned}\boldsymbol{P} &= \frac{\partial W_T}{\partial \boldsymbol{F}}\\ &= \sum_{K=1}^{6}\left(\frac{1}{2\Omega_0}\sum_{J=1}^{6}\frac{\partial U_{\mathrm{WLC}}(|\boldsymbol{r}_{IJ}|)}{\partial \boldsymbol{r}_{IK}} + \frac{1}{3\Omega_0}\sum_{\gamma=1}^{6}\frac{\partial U_{\mathrm{S}}(A_\gamma)}{\partial \boldsymbol{r}_{IK}}\right)\\ &\quad\otimes\boldsymbol{R}_{IK},\end{aligned} \tag{6}$$

$$\boldsymbol{Q} = \frac{\partial W_T}{\partial \boldsymbol{G}} = \frac{1}{2}\sum_{K=1}^{6}\left(\frac{1}{2\Omega_0}\sum_{J=1}^{6}\frac{\partial U_{\mathrm{WLC}}(|\boldsymbol{r}_{IJ}|)}{\partial \boldsymbol{r}_{IK}} + \frac{1}{3\Omega_0}\sum_{\gamma=1}^{6}\frac{\partial U_{\mathrm{S}}(A_\gamma)}{\partial \boldsymbol{r}_{IK}}\right) \otimes \boldsymbol{R}_{IK} \otimes \boldsymbol{R}_{IK}, \tag{7}$$

where the subscripts I, J, and K denote the junction points.

Furthermore, the tangent modulus tensors can be obtained from the second-order partial derivatives of the free energy density with respect to the deformation gradient tensors $\boldsymbol{F}$ and $\boldsymbol{G}$ as

$$\boldsymbol{M}_{FF} = \frac{\partial^2 W_T}{\partial \boldsymbol{F} \otimes \partial \boldsymbol{F}} = \sum_{K=1}^{6}\sum_{L=1}^{6}\left(\frac{1}{2\Omega_0}\sum_{J=1}^{6}\frac{\partial^2 U_{\mathrm{WLC}}(|\boldsymbol{r}_{IJ}|)}{\partial \boldsymbol{r}_{IK} \otimes \partial \boldsymbol{r}_{IL}} + \frac{1}{3\Omega_0}\sum_{\gamma=1}^{6}\frac{\partial^2 U_{\mathrm{S}}(A_\gamma)}{\partial \boldsymbol{r}_{IK} \otimes \partial \boldsymbol{r}_{IL}}\right)\underline{\otimes}(\boldsymbol{R}_{IK} \otimes \boldsymbol{R}_{IL}), \tag{8}$$

$$\boldsymbol{M}_{FG} = \frac{\partial^2 W_T}{\partial \boldsymbol{F} \otimes \partial \boldsymbol{G}} = \frac{1}{2}\sum_{K=1}^{6}\sum_{L=1}^{6}\left[\left(\frac{1}{2\Omega_0}\sum_{J=1}^{6}\frac{\partial^2 U_{\mathrm{WLC}}(|\boldsymbol{r}_{IJ}|)}{\partial \boldsymbol{r}_{IK} \otimes \partial \boldsymbol{r}_{IL}} + \frac{1}{3\Omega_0}\sum_{\gamma=1}^{6}\frac{\partial^2 U_{\mathrm{S}}(A_\gamma)}{\partial \boldsymbol{r}_{IK} \otimes \partial \boldsymbol{r}_{IL}}\right)\underline{\otimes}(\boldsymbol{R}_{IK} \otimes \boldsymbol{R}_{IL})\right] \otimes \boldsymbol{R}_{IL}, \tag{9}$$

$$\boldsymbol{M}_{GF} = \frac{\partial^2 W_T}{\partial \boldsymbol{G} \otimes \partial \boldsymbol{F}} = \frac{1}{2}\sum_{K=1}^{6}\sum_{L=1}^{6}\left[\left(\frac{1}{2\Omega_0}\sum_{J=1}^{6}\frac{\partial^2 U_{\mathrm{WLC}}(|\boldsymbol{r}_{IJ}|)}{\partial \boldsymbol{r}_{IK} \otimes \partial \boldsymbol{r}_{IL}} + \frac{1}{3\Omega_0}\sum_{\gamma=1}^{6}\frac{\partial^2 U_{\mathrm{S}}(A_\gamma)}{\partial \boldsymbol{r}_{IK} \otimes \partial \boldsymbol{r}_{IL}}\right)\bar{\otimes}(\boldsymbol{R}_{IK} \otimes \boldsymbol{R}_{IK})\right] \otimes \boldsymbol{R}_{IL}, \tag{10}$$

$$\boldsymbol{M}_{GG} = \frac{\partial^2 W_T}{\partial \boldsymbol{G} \otimes \partial \boldsymbol{G}} = \frac{1}{2}\sum_{K=1}^{6}\sum_{L=1}^{6}\left[\left(\frac{1}{2\Omega_0}\sum_{J=1}^{6}\frac{\partial^2 U_{\mathrm{WLC}}(|\boldsymbol{r}_{IJ}|)}{\partial \boldsymbol{r}_{IK} \otimes \partial \boldsymbol{r}_{IL}} + \frac{1}{3\Omega_0} \times \sum_{\gamma=1}^{6}\frac{\partial^2 U_{\mathrm{S}}(A_\gamma)}{\partial \boldsymbol{r}_{IK} \otimes \partial \boldsymbol{r}_{IL}}\right)\bar{\otimes}(\boldsymbol{R}_{IK} \otimes \boldsymbol{R}_{IK})\right] \otimes (\boldsymbol{R}_{IL} \otimes \boldsymbol{R}_{IL}), \tag{11}$$

where $[\boldsymbol{A}\underline{\otimes}\boldsymbol{B}]_{ijkl} = A_{ik}B_{jl}$, $[\boldsymbol{A}\bar{\otimes}\boldsymbol{B}]_{ijkl} = A_{il}B_{jk}$. The summation is not implied on the indices I, J, and K. Obviously, it is a hyperelastic constitutive model and subsequently it will be employed to characterize the nonlinear mechanical properties of RBC membrane.

The In-Plane Elastic Properties of RBC Membrane

Based on the hyperelastic constitutive model established above, with use of the semi-analytical method, several in-plane elastic properties such as Young's modulus, Poisson's ratio, shear modulus, and area compression modulus of RBC membrane under uniform axial tension are investigated systematically in this section.

As shown by Zhang et al. (2002), in the context QC framework, the Young's modulus and Poisson's ratio of thin film/membrane can be calculated by the following forms, respectively,

$$E = (\boldsymbol{M}_{FF})_{1111} - \frac{(\boldsymbol{M}_{FF})_{1122}^2}{(\boldsymbol{M}_{FF})_{2222}}, \tag{12a}$$

$$v = \frac{(\boldsymbol{M}_{FF})_{1122}}{(\boldsymbol{M}_{FF})_{1111}}, \tag{12b}$$

The shear modulus and area compression modulus of RBC membrane can be obtained by the following relationships, respectively,

$$K_0 = \frac{(\boldsymbol{M}_{FF})_{2222} + (\boldsymbol{M}_{FF})_{1122}}{2}, \tag{13a}$$

$$\mu_0 = \frac{(\boldsymbol{M}_{FF})_{2222} - (\boldsymbol{M}_{FF})_{1122}}{2}. \tag{13b}$$

Firstly, we selected a planar equivalent continuum membrane with the spectrin network with the length L and width H as the reference configuration (see Fig. 3 for reference). Obviously, the first-order deformation gradient tensors of the membrane subjected to uniform axial tension along the horizontal direction has the following form

$$F_{ij} = \begin{bmatrix} \lambda_1 & 0 \\ \lambda_1\beta & \lambda_2 \end{bmatrix}, \tag{14}$$

where λ_1, λ_2, and β denoting the longitudinal relaxation parameter, the lateral relaxation parameter, and the shear strain, respectively. Clearly, the second-order deformation gradient tensor $\boldsymbol{G}$ vanishes in this in-plane homogeneous

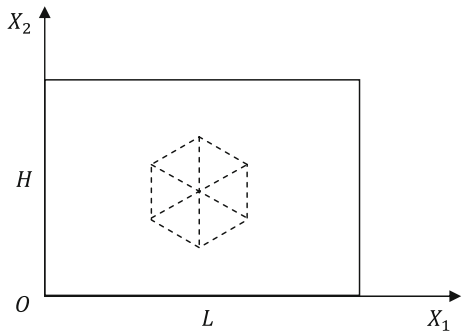

Fig. 3 Schematic illustration of the rectangular equivalent RBC membrane with zigzag chirality

deformation case (it works in nonhomogeneous deformation, see "Meshless Numerical Computational Scheme" and "Numerical Examples and Discussion"). From Eq. (14), the free energy density $W_T(\boldsymbol{F},\boldsymbol{G})$ in Eq. (1) can be rewrited as $W_T(\lambda_1,\lambda_2,\beta)$ and the minimization of the free energy density with respect to these parameters can be given as

$$\frac{\partial W_T}{\partial \lambda_1}=\frac{\partial W_T}{\partial \lambda_2}=\frac{\partial W_T}{\partial \beta}=0. \tag{15}$$

Subsequently, the bisection method is applied to determine the minimum of the free energy. The structural parameters of RBC membrane are taken as $p=8.5\,\text{nm}$, $a_0=87\,\text{nm}$, and $a_{\max}=238\,\text{nm}$ in the following study. The chiral angle θ of RBC membranes can be defined as that of graphene sheet, i.e., θ ranges from 0° for zigzag to 30° for armchair (the illustration of equivalent RBC membrane in Fig. 3 is a zigzag membrane). The system temperature is chosen as 300 K.

Table 1 shows the optimization parameters λ_1, λ_2, and β of RBC membrane sheets with different chiral angles 0°, 15°, and 30°, respectively, under axial tension deformation at 300 K. It can be found that with the increase of the λ_1, i.e., with the increasing axial tension deformation, the λ_2 for RBC membranes with different chiral angles decreases gradually; however, the amount of decrease is different. The parameter β remains unchanged for RBC membranes with 0° and 30° chiral angle, but increases for 15° chiral angle. It means that the mechanical properties of RBC membrane can be determined by both the amount of deformation and its chirality. For obtained further details, five types of RBC membranes with 0°, 7.5°, 15°, 22.5°, and 30° chiral angle, respectively, are investigated here.

Figure 4 shows the variation of Young's moduli of RBC membranes with different chirality versus axial tensile strain at 300 K. It can be found that although the Young's moduli have slightly decrease when the axial tensile strain $\varepsilon \le 0.3$, the variations of the Young's moduli are quite gentle and the difference between Young's moduli for different chiral angles are pretty small. However, when $\varepsilon > 0.3$, the Young's moduli increase rapidly with the increasing of the deformation and the difference between the Young's moduli for five types of RBC membranes becomes larger. For example, the Young's moduli are 18.5, 18.6, 18.8, 18.9, and 19.0 μN/m for RBC membranes with chiral angles of 0°, 7.5°, 15°, 22.5°, and 30°, respectively, at $\varepsilon = 0.3$, while those are 29.5, 30.6, 33.3, 36.3, and 37.6 μN/m for chiral angles of 0°, 7.5°, 15°, 22.5°, and 30°, respectively, at $\varepsilon = 0.8$. These datum suggest that the axial tensile strain and chiral angle have little effect on the Young's moduli when $\varepsilon \le 0.3$, but, as long as $\varepsilon > 0.3$, they both have an increasing effect on the Young's moduli. Figure 5 shows the dependence of the Poisson's ratio on the chirality of RBC membrane at different axial tension strain at 300 K. Obviously, the Poisson's ratios decrease rapidly from 1/3 with the increasing of the deformation. Simultaneously, the chirality also has a declining effect on

Table 1 The optimization parameters λ_1, λ_2, and β of RBC membranes with different chiral angles 0°, 15°, and 30°, respectively, under axial tension deformation at 300 K

λ_1 (0°)	λ_2 (0°)	β (0°)	λ_1 (15°)	λ_2 (15°)	β (15°)	λ_1 (30°)	λ_2 (30°)	β (30°)
1	1	1.04E−17	1	1	1.04E−17	1	1	1.04E−17
1.05	0.98373	1.04E−17	1.05	0.98375	3.88E−05	1.05	0.98376	1.04E−17
1.1	0.96820	1.04E−17	1.1	0.96825	0.00018	1.1	0.96830	1.04E−17
1.15	0.95332	1.04E−17	1.15	0.95343	0.00044	1.15	0.95355	1.04E−17
1.2	0.93901	1.04E−17	1.2	0.93922	0.00089	1.2	0.93943	1.04E−17
1.25	0.92521	1.04E−17	1.25	0.92555	0.00156	1.25	0.92589	1.04E−17
1.3	0.91186	1.04E−17	1.3	0.91236	0.00251	1.3	0.91287	1.04E−17
1.35	0.89889	1.04E−17	1.35	0.89959	0.00381	1.35	0.90032	1.04E−17
1.4	0.88625	1.04E−17	1.4	0.88721	0.00555	1.4	0.88821	1.04E−17
1.45	0.87390	1.04E−17	1.45	0.87516	0.00782	1.45	0.87650	1.04E−17
1.5	0.86178	1.04E−17	1.5	0.86340	0.01074	1.5	0.86515	1.04E−17
1.55	0.84985	1.04E−17	1.55	0.85189	0.01441	1.55	0.85413	1.04E−17
1.6	0.83808	1.04E−17	1.6	0.84058	0.01901	1.6	0.84342	1.04E−17
1.65	0.82640	1.04E−17	1.65	0.82945	0.02469	1.65	0.8330	1.04E−17
1.7	0.81478	1.04E−17	1.7	0.81844	0.03166	1.7	0.82283	1.04E−17
1.75	0.80317	1.04E−17	1.75	0.80752	0.04014	1.75	0.81291	1.04E−17
1.8	0.79153	1.04E−17	1.8	0.79663	0.05038	1.8	0.80321	1.04E−17
1.85	0.77981	1.04E−17	1.85	0.78571	0.06268	1.85	0.79371	1.04E−17
1.9	0.76795	1.04E−17	1.9	0.77473	0.07737	1.9	0.78441	1.04E−17
1.95	0.75589	1.04E−17	1.95	0.76359	0.09483	1.95	0.77528	1.04E−17

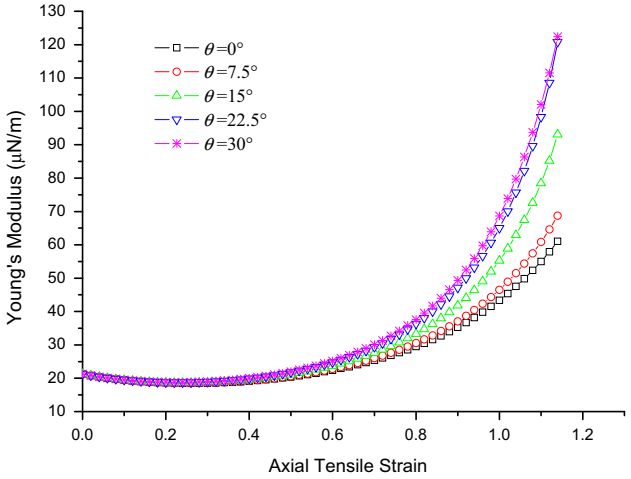

Fig. 4 The Young's moduli of RBC membranes with different chirality under axial tension deformation at 300 K

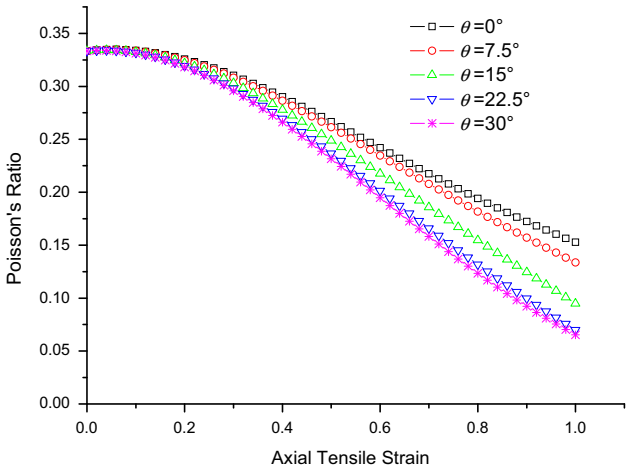

Fig. 5 The Poisson's ratio of RBC membranes with different chirality under axial tension deformation at 300 K

the Poisson's ratio and the drops become larger with the deformation increasing.

The relationships between area compression moduli of RBC membrane sheets with different chirality and the axial tensile strain at 300 K are given in Fig. 6. Like the variation tendency of Young's modulus in Fig. 4, the axial tensile strain of about 0.3 is also the critical strain for the area compression modulus-axial tensile strain curves which is consistent with that reported by Dao et al. (2006). For the case of $\varepsilon = 0.3$, the area compression moduli are 15.03, 15.02, 14.98, 14.95, and 14.94 μN/m for RBC membranes with chiral angles of 0°, 7.5°, 15°, 22.5°, and 30°, respectively, and the values are 15.83, 15.69, 15.33, 14.93, and 14.76 μN/m for chiral angles of 0°, 7.5°, 15°, 22.5°, and 30°, respectively, at $\varepsilon = 0.8$. As a whole, the chiral angle has a decreasing effect on the area compression

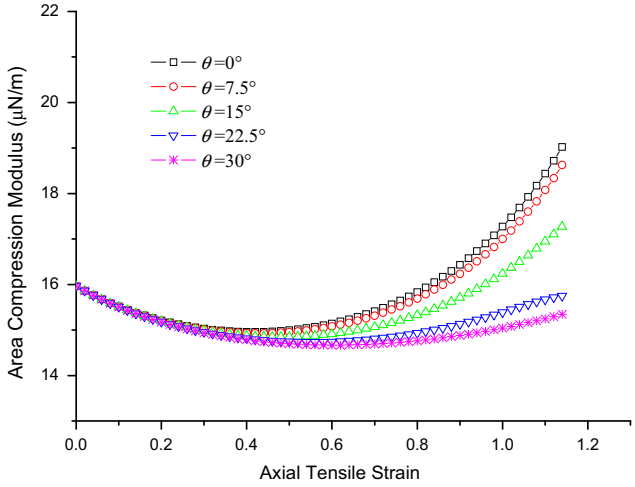

Fig. 6 The area compression moduli of RBC membranes with different chirality under axial tension deformation at 300 K

moduli and the drops become larger with the deformation increasing.

In order to have a further understanding of the mechanical properties of RBC membrane, the shear modulus is also studied thoroughly. Figure 7 shows the dependence of the shear modulus on the chiral angle of RBC membrane at different axial tension strain at 300 K. It is found that the shear moduli increase almost linearly with the axial strain when about $\varepsilon \leq 0.3$. However, after the critical point $\varepsilon = 0.3$, an interesting variation of shear modulus can be observed. The shear moduli of RBC membranes with chiral angles 0° and 30°, respectively, remain almost linear increasing trend, but the other shear moduli present approximate quadratic functions of ε. It suggests that chiral angle has a great influence on the shear moduli. Figure 8

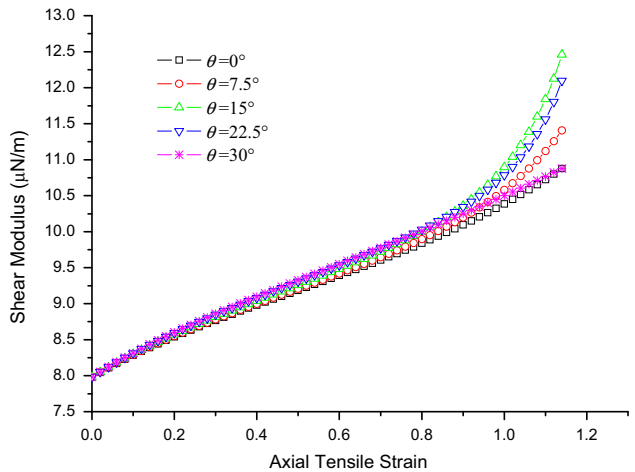

Fig. 7 The shear moduli of RBC membranes with different chirality under axial tension deformation at 300 K

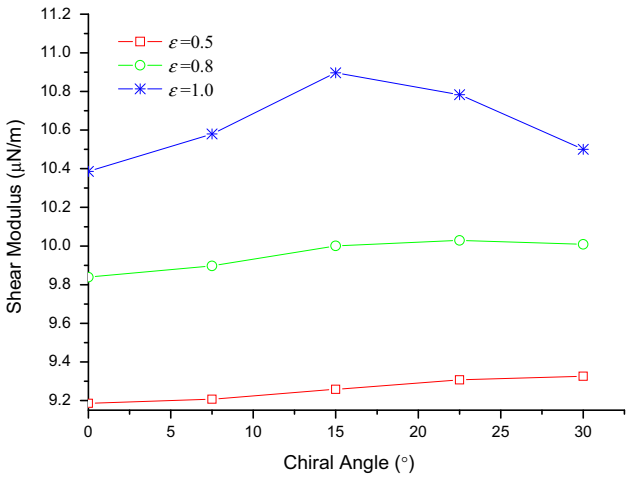

Fig. 8 The shear moduli of different chiral RBC membranes versus the chiral angle at 300 K

demonstrates the effect of the chirality on the shear moduli at 300 K. From Figs. 7 and 8, it can be observed that, when about $\varepsilon < 0.8$, the shear moduli increase with the increasing of chiral angle, however, as long as $\varepsilon > 0.8$, the shear moduli first increase and then decline as the chiral angle increases and the peak value appears at $\theta = 15°$. In a word, the shear modulus of RBC membrane is sensitive to the chiral angle at large deformation.

In summary, from Figs. 4, 5, 6, 7, and 8, the mechanical properties of RBC membrane exhibit nonlinear changes during deformation and the mechanical properties of RBC membrane are almost insensitive to chiral angles when about $\varepsilon \leq 0.3$, i.e., it exhibits isotropic material properties; however, at larger deformation ($\varepsilon > 0.3$), the anisotropic material properties of RBC membrane become dramatically.

Meshless Numerical Computational Scheme

Based on the constructed QC hyperelastic constitutive model, a meshless numerical simulation framework is established for predicting complex nonhomogeneous deformation patterns of RBC membrane fragments in this section. As the free energy density of RBC membrane is a function of the first- and second-order deformation gradient tensor, the numerical interpolation must require at least C^1-continuity. In the present paper, the meshless element-free Galerkin method (Dolbow and Belytschko 1998) on the basis of the moving least-squares approximation (Lancaster and Salkauskas 1981) is utilized for the implementation of the numerical computation.

Based on the QC constitutive model, the total free energy Π_{tot} of the considered RBC membrane fragment with prescribed natural and essential boundary conditions can be expressed as

$$\begin{aligned}\prod\nolimits_{\text{tot}} = &\int_{\Omega_0} W_T(\boldsymbol{F},\boldsymbol{G})\mathrm{d}\Omega - \int_{\Omega_0} \boldsymbol{u}\cdot\boldsymbol{b}_0\mathrm{d}\Omega - \int_{\Gamma_t} \boldsymbol{u}\cdot\boldsymbol{t}_0^P\mathrm{d}S \\ &- \int_{\Gamma_t} \nabla_N\boldsymbol{u}\cdot\boldsymbol{t}_0^Q\mathrm{d}S + \frac{1}{2}\int_{\Gamma_u}\gamma(\boldsymbol{u}-\tilde{\boldsymbol{u}})\cdot(\boldsymbol{u}-\tilde{\boldsymbol{u}})\mathrm{d}S,\end{aligned} \tag{16}$$

where $\boldsymbol{b}_0$, $\boldsymbol{t}_0^P$, and $\boldsymbol{t}_0^Q$ denote the body force density, boundary traction, and boundary couple, respectively. Ω_0 is the domain occupied by the initial planar/reference configuration. Γ_t and Γ_u are the traction and displacement boundary, respectively. $\nabla_N\{\circ\} = \nabla_X\{\circ\}\cdot\boldsymbol{N}$, whereby $\nabla_X\{\circ\}$ denotes the left gradient operator with respect to the material placement $\boldsymbol{X}$ and $\boldsymbol{N}$ denotes the normal vector to surface Γ_t. γ is the penalty factor. $\tilde{\boldsymbol{u}} = (\tilde{u}_1,\tilde{u}_2,\tilde{u}_3)^{\mathrm{T}}$ represents the boundary displacement on the surface Γ_u. $\boldsymbol{u} = (u_1,u_2,u_3)^{\mathrm{T}}$ represents the displacement field of the equivalent continuum RBC membrane, for the numerical computation, which can be calculated from the moving least-squares approximation as

$$\boldsymbol{u}(\boldsymbol{X}) = \sum_{I=1}^{N}\phi_I(\boldsymbol{X})\hat{\boldsymbol{u}}^I, \tag{17}$$

with $\hat{\boldsymbol{u}}^I = \left(\hat{u}_1^I,\hat{u}_2^I,\hat{u}_3^I\right)^{\mathrm{T}}$ denoting the nodal displacement parameter vector associated with meshless node I and ϕ_I denoting the meshless shape function of Ith node which is constructed on the corresponding two-dimensional domain with the material coordinate $\boldsymbol{X} = (X_1,X_2)^{\mathrm{T}}$.

Bearing in mind Eq. (17), the first- and second-order deformation gradient tensors in Eq. (16) can be derived in the following way

$$\boldsymbol{F} = \frac{\partial\boldsymbol{\varphi}(\boldsymbol{X})}{\partial\boldsymbol{X}} + \frac{\partial\boldsymbol{u}(\boldsymbol{X})}{\partial\boldsymbol{X}} = \frac{\partial\boldsymbol{\varphi}(\boldsymbol{X})}{\partial\boldsymbol{X}} + \sum_{I=1}^{N}\frac{\partial\phi_I}{\partial\boldsymbol{X}}\otimes\hat{\boldsymbol{u}}^I, \tag{18}$$

$$\begin{aligned}\boldsymbol{G} &= \frac{\partial^2\boldsymbol{\varphi}(\boldsymbol{X})}{\partial\boldsymbol{X}\otimes\partial\boldsymbol{X}} + \frac{\partial^2\boldsymbol{u}(\boldsymbol{X})}{\partial\boldsymbol{X}\otimes\partial\boldsymbol{X}} \\ &= \frac{\partial^2\boldsymbol{\varphi}(\boldsymbol{X})}{\partial\boldsymbol{X}\otimes\partial\boldsymbol{X}} + \sum_{I=1}^{N}\frac{\partial^2\phi_I}{\partial\boldsymbol{X}\otimes\partial\boldsymbol{X}}\otimes\hat{\boldsymbol{u}}^I,\end{aligned} \tag{19}$$

where $\boldsymbol{\varphi}(\boldsymbol{X}) = (\varphi_1(\boldsymbol{X}),\varphi_2(\boldsymbol{X}),\varphi_3(\boldsymbol{X}))^{\mathrm{T}}$ denotes the transformation mapping from the reference planar configuration to the quasi-planar structure.

With the assumption that the fields included in Π_{tot} are sufficiently smooth, the variation of Π_{tot} associated with $\delta\boldsymbol{u}$ can be expressed as

$$\begin{aligned}\delta\Pi_{\mathrm{tot}}(\boldsymbol{u};\delta\boldsymbol{u}) &= \int_{\Omega_0}\boldsymbol{P}:\delta\boldsymbol{F}\mathrm{d}\Omega+\int_{\Omega_0}\boldsymbol{Q}\vdots\delta\boldsymbol{G}\mathrm{d}\Omega\\ &-\int_{\Omega_0}\delta\boldsymbol{u}\cdot\boldsymbol{b}_0\mathrm{d}\Omega-\int_{\Gamma_t}\delta\boldsymbol{u}\cdot\boldsymbol{t}_0^P\mathrm{d}S-\int_{\Gamma_t}\nabla_N\delta\boldsymbol{u}\cdot\boldsymbol{t}_0^Q\mathrm{d}S\\ &+\int_{\Gamma_u}\gamma(\boldsymbol{u}-\tilde{\boldsymbol{u}})\cdot\delta\boldsymbol{u}\mathrm{d}S\\ &=\int_{\Omega_0}\sum_{I=1}^{N}\left(\boldsymbol{P}\cdot\nabla_X\phi_I+\boldsymbol{Q}:\nabla_{XX}\phi_I\cdot\delta\hat{\boldsymbol{u}}^I\mathrm{d}\Omega\right)\\ &-\int_{\Omega_0}\sum_{I=1}^{N}\phi_I\boldsymbol{b}_0\cdot\delta\hat{\boldsymbol{u}}^I\mathrm{d}\Omega\\ &-\int_{\Gamma_t}\sum_{I=1}^{N}\phi_I\boldsymbol{t}_0^P\cdot\delta\hat{\boldsymbol{u}}^I\mathrm{d}S-\int_{\Gamma_t}\sum_{I=1}^{N}\boldsymbol{N}\cdot\nabla_X\phi_I\otimes\delta\hat{\boldsymbol{u}}^I\cdot\boldsymbol{t}_0^Q\mathrm{d}S\\ &+\int_{\Gamma_u}\sum_{I=1}^{N}\gamma\phi_I(\boldsymbol{u}-\tilde{\boldsymbol{u}})\cdot\delta\hat{\boldsymbol{u}}^I\mathrm{d}S=0,\end{aligned}\tag{20}$$

where $\nabla_X\phi_I$ and $\nabla_{XX}\phi_I$ denote the first- and second-order gradient of ϕ_I with respect to $\boldsymbol{X}$, respectively.

From Eq. (20), the resulting incremental stiffness equation can be obtained as

$$(\boldsymbol{K}_0(\hat{\boldsymbol{u}}_n)+\boldsymbol{K}^\gamma)\cdot(\hat{\boldsymbol{u}}_{n+1}-\hat{\boldsymbol{u}}_n)=-\boldsymbol{P}_0(\hat{\boldsymbol{u}}_n)-(\boldsymbol{K}^\gamma\cdot\hat{\boldsymbol{u}}_n-\boldsymbol{P}^\gamma),\tag{21}$$

where $\hat{\boldsymbol{u}}_n$ and $\hat{\boldsymbol{u}}_{n+1}$ are the displacement parameters in the n and $n+1$ iteration step, respectively. And

$$\boldsymbol{K}_0=\int_{\Omega_0}\begin{pmatrix}\boldsymbol{M}_{FF}:\nabla_X\phi_I\otimes\nabla_X\phi_J+\boldsymbol{M}_{FG}\vdots\nabla_X\phi_I\otimes\nabla_{XX}\phi_J+\boldsymbol{M}_{GF}\\ \vdots\nabla_{XX}\phi_I\otimes\nabla_X\phi_J+\nabla_{XX}\phi_I:\boldsymbol{M}_{GF}:\nabla_{XX}\phi_J\end{pmatrix}\mathrm{d}\Omega,\tag{22}$$

$$\begin{aligned}\boldsymbol{P}_0&=\int_{\Omega_0}(\boldsymbol{P}\cdot\nabla_X\phi_I+\boldsymbol{Q}:\nabla_{XX}\phi_J)\mathrm{d}\Omega-\int_{\Omega_0}\boldsymbol{b}_0\phi_I\mathrm{d}\Omega\\ &-\int_{\Gamma_t}\boldsymbol{t}_0^P\phi_I\mathrm{d}S-\int_{\Gamma_t}\boldsymbol{t}_0^Q(\boldsymbol{N}\cdot\nabla_X\phi_I)\mathrm{d}S,\end{aligned}\tag{23}$$

$$\boldsymbol{K}^\gamma=\int_{\Gamma_u}\gamma\phi_I\phi_J{}^2\mathbf{1}\mathrm{d}S\tag{24}$$

$$\boldsymbol{P}^\gamma=\int_{\Gamma_u}\gamma\phi_I\tilde{\boldsymbol{u}}\mathrm{d}S,\tag{25}$$

where ${}^2\mathbf{1}$ denotes the second-order identity tensor. The Newton–Raphson iteration will be used to find the equilibrium configuration of RBC membranes at prescribed boundary conditions in an increment way.

Numerical Examples and Discussion

In this section, nonhomogeneous large deformation of rectangular RBC membrane fragments under tensile and shear loadings (displacement) at room temperature (300 K) are simulated with use of the established meshless numerical scheme. Herein, before computation, a quasi-planar sheet with an extremely large cylindrical radius compared with the fragment geometry is introduced. This simple treatment as a role of perturbation can help to obtain equilibrium out-of-plane deformation patterns easily. The transformation mapping from the planar membrane (the reference configuration) to the corresponding quasi-planar configuration (the undeformed membrane) can be defined as

$$\varphi_1=X_1,\tag{26a}$$

$$\varphi_2=R\sin\left(\frac{X_2}{R}\right),\tag{26b}$$

$$\varphi_3=R\left(1-\cos\left(\frac{X_2}{R}\right)\right),\tag{26c}$$

with R denoting the curvature radius of the quasi-planar fragment.

In the following examples, the isothermal and quasi-static conditions are assumed. The structure parameters are taken as $p=8.5$ nm, $a_0=87$ nm, and $a_{\max}=238$ nm. The essential boundary conditions are treated by means of penalty function method. The symbol $m\times n$ used in the following examples denotes the total number of the meshless nodes involved in the following numerical computations, whereby m nodes are distributed evenly along the longitudinal direction and n nodes are collocated uniformly along the lateral direction of the planar equivalent RBC membrane model.

Before loading, through energy minimization, the initial equilibrium configuration of RBC membrane sheet can be obtained from the quasi-planar counterpart. Taking the square RBC membrane sheet with the edge length of 50.0 nm and $R=1.0\times10^8$ nm as an example, with two opposite edges are clamped, the value of average energy density of the RBC membrane sheet converges to 0.54778 kg nm^2/s^2 which is smaller than 0.55254 kg nm^2/s^2 for the quasi-planar configuration (the planar counterpart is also about 0.55254 kg nm^2/s^2). The quasi-planar and the equilibrium configurations are displayed in Fig. 9. It can be seen that the free sides, the right and left edges, of the

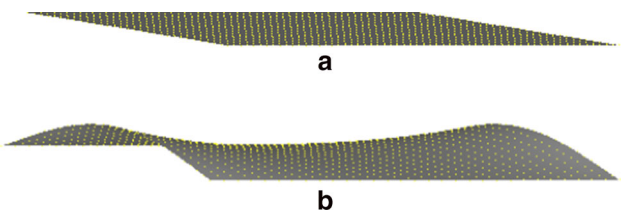

Fig. 9 The square RBC membrane sheet with the edge length of 50.0 nm and $R=1.0\times10^8$ nm: **a** the quasi-planar configuration, **b** the equilibrium configuration

equilibrium RBC membrane curl inward to form a saddle shape and the width of its central part shrinks slightly. This indicates that the saddle-shaped RBC membrane is more stable than its planar and quasi-planar counterparts.

Stretched RBC Membrane

In this example, the large deformation of a square RBC membrane fragment subjected to axial tension at 300 K is simulated with use of the established meshless numerical framework. The length of the side of the considered square RBC membrane is taken as 50.0 nm and the curvature radius R is chosen as 1.0×10^8 nm. The number of the meshless nodes used in the present numerical computation is chosen as 30×30. The left edge of the RBC membrane is fixed and the horizontal stretch displacement is imposed on the clamped right edge gradually at 1.0 nm per step.

Firstly, the influence of chirality on the deformation of the considered RBC membrane fragment is studied. The variations of the average strain energy of the RBC membranes with different chiral angles versus the axial tensile strain at 300 K are depicted in Fig. 10. It can be found that the average strain energy increases approximately as a quadratic function of the tensile strain. As expected, at the initial stage of deformation, chirality has little impact on the deformation of RBC membrane, however, as the deformation continues to increase, the increasing effect of chirality can be observed clearly. The deformation patterns of the RBC membrane sheet with chiral angle of 0° at $\varepsilon = 0.4$ and $\varepsilon = 1.0$, respectively, are demonstrated in Fig. 11.

As mentioned above, the standard CB rule only involving the first-order deformation gradient tensor cannot be used to account for the curvature effect of 2D nanoscale membrane exactly. Fortunately, the HCB rule with the second-order deformation gradient tensor included can remedy this defect which has been confirmed by Sun and Liew (2008). The effect of second-order deformation gradient tensor on the deformation of RBC membrane is also investigated in the present paper. Figure 12 shows the variations of the average strain energy with respect to the axial tension strain of the RBC membrane sheet with the

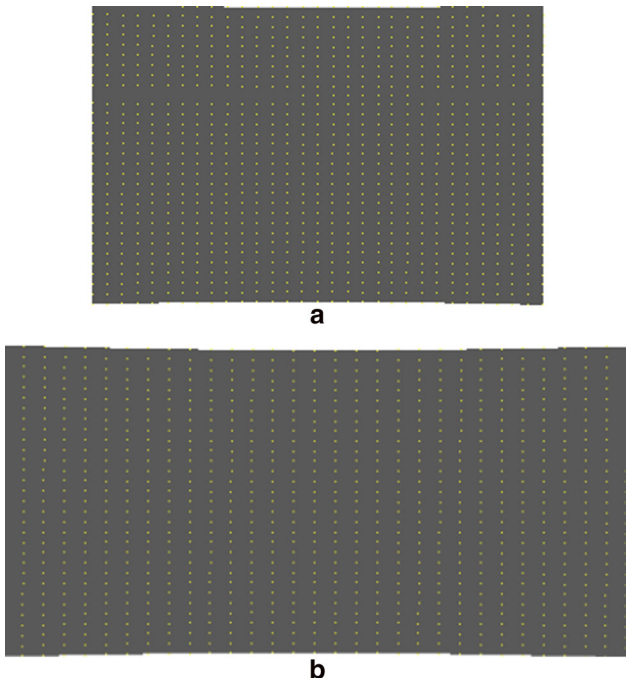

Fig. 11 The deformation patterns of the RBC membrane sheet with the chiral angle of 0° at 300 K under tension: **a** at $\varepsilon = 0.5$ and **b** at $\varepsilon = 1.0$

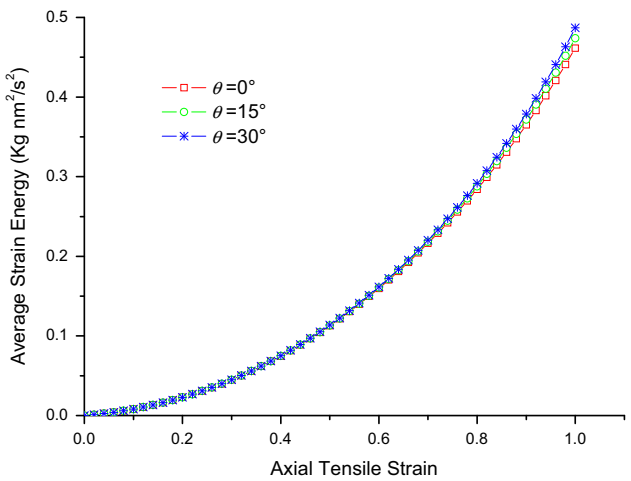

Fig. 10 The relationships between the average strain energy and the axial tensile strain of RBC membrane sheets with chiral angles of 0°, 15°, and 30°, respectively, at 300 K

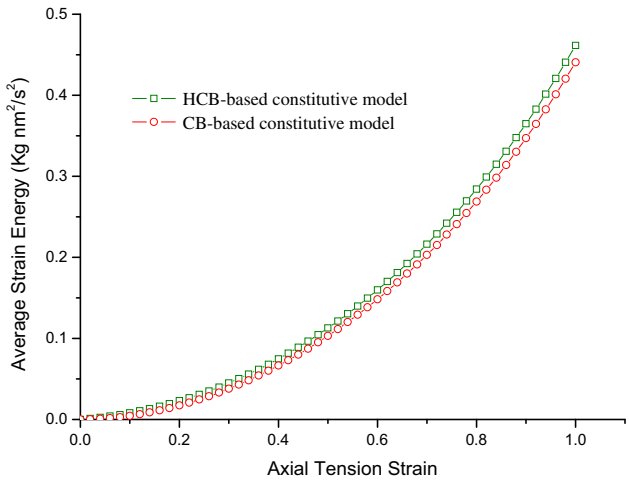

Fig. 12 The variations of the average strain energy with respect to the axial tension strain of the RBC membrane sheet with the chiral angle of 0° at 300 K

chiral angle of 0° at 300 K obtained by the HCB-based and the CB-based model, respectively. As a whole, the growth of the average strain energy changes nearly quadratically with the increase of the tension. The average strain energy obtained with use of the CB-based constitutive model is slightly smaller than that from HCB-based constitutive model at early deformation stage. And then, the distinction becomes larger with the deformation continually increasing. It seems that without the second-order deformation gradient tensor, the CB-based RBC membrane model is 'softer' than the HCB-based model since the bending stiffness induced by curvature cannot be described accurately, especially at large deformation. Obviously, although RBC membrane is a soften material, the curvature effect should be taken into consideration.

Sheared RBC Membrane

In this example, the wrinkling/buckling behavior of RBC membrane upon large shear loading at 300 K is studied based on the proposed meshless numerical scheme. The length and width of the considered rectangular RBC membrane patch is chosen as 35 and 25 nm, respectively, with $R = 1.0 \times 10^8$ nm. The left edge (i.e., the long side) of the RBC membrane is fixed and the loadings (displacement) are enforced on the right edge. Herein, firstly, a 28 % in-plane pre-stretching is imposed on the right edge of the membrane to give it a preliminary stiffness before shearing. Subsequently, the shear displacement is enforced on the right edge along the longitudinal direction at 0.5 nm per step.

With 21 × 29 meshless nodes applied, the shear deformation behaviors of the considered RBC membrane are simulated. The variations of the average strain energy associated with the shear strain are shown in Fig. 13. It can be seen that when the shear strain is smaller than about 0.8, the values of average strain energy for the RBC membrane models with different chiral angles are almost consistent with each other. However, as long as exceeded this threshold, the increasing effect of chirality on the average shear strain energy can be observed clearly. This trend is in agreement with that from semi-analytical method (Wang et al. 2014) and that given by Dao et al. (2006) based on the molecularly based model. Figure 14 depicts the curves of the average strain energy versus the shear strain for the RBC membrane sheet with the chiral angle of 0° based on HCB rule and CB rule- based model, respectively. Like that shown in Fig. 12, as a whole, the values of the average strain energy predicted by the CB-based RBC membrane model are smaller than those from HCB-based model and the difference between them becomes larger as the deformation increases. The corresponding out-of-plane wrinkling patterns of the RBC membrane with the chiral angle of 0° at shear strain of 1.0 are presented in Fig. 15. Obviously, three folds developed in one diagonal direction with use of HCB-based rule, however, four large folds and two smaller ones are observed from CB-based model. It can be further confirmed that, without higher order deformation gradient involved, the bending stiffness depended on the curvature of RBC membrane cannot be considered correctly. Note that, unlike other nanomaterials such as carbon-based structures (Wang and Guo 2012; Yan et al. 2013), although buckling patterns appear during the deformation, it could hardly find energy sudden jumps in the average strain energy-shear strain curve. It could be explained that RBC membrane is much more soften than carbon materials.

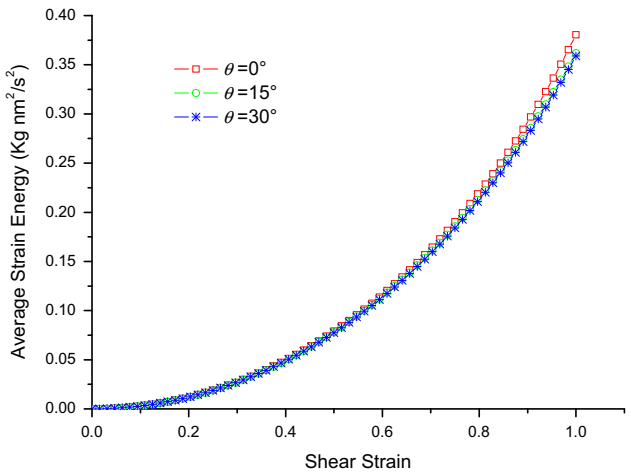

Fig. 13 The average strain energy for RBC membrane sheets with respect to the shear strain at 300 K

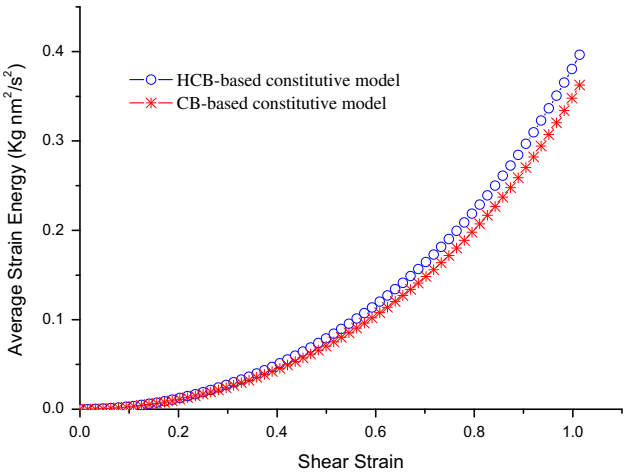

Fig. 14 The average strain energy versus average shear strain for the RBC membrane sheet with the chiral angle of 0° at 300 K

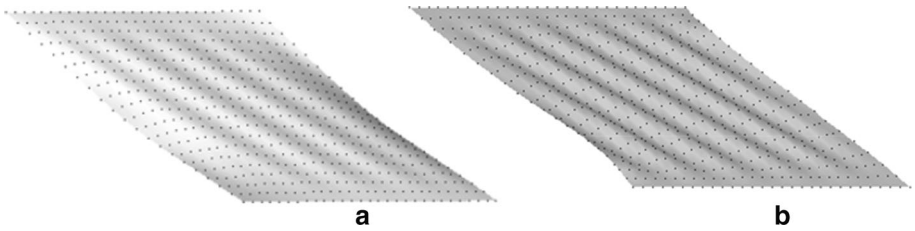

Fig. 15 The wrinkling patterns the RBC membrane sheet with the chiral angle of 0° at shear strain of 1.0 predicted numerically by **a** the HCB rule-based model and **b** the CB rule based model, respectively, at 300 K

Concluding Remarks

In the present paper, the WLC-based symmetrical hexagonal lattice model is utilized to characterize the RBC membrane. Based on this simplified parameterized membrane model, a QC formulation and the corresponding meshless simulation scheme are established for the mechanical and large deformation properties of RBC membrane at 300 K. The research results suggest that RBC membrane is a nonlinear hyperelastic material, and RBC membrane presents isotropic nature in the case of smaller deformation, however, as the deformation continues increase, its anisotropic material properties become dramatically. The out-of-plane wrinkling of RBC membrane subjected to shear loading can be reproduced during the meshless numerical simulation. With the involvement of the second-order deformation gradient tensor in the constitutive model, the bending stiffness of RBC membrane can be taken into account in a convenient way.

Acknowledgments The financial support from the Promotive Research Fund for Excellent Young and Middle-aged Scientists of Shandong Province, China (BS2014SF004), the Doctoral Starting up Foundation of Ludong University, China (LY2014022), the National Science Foundation of China (11372281), the province Science Foundation of Zhejiang (Y13A020009), and Natural Science Fund of Shandong Province (ZR2013EEL007) are gratefully acknowledged.

References

An XL, Mohandas N (2008) Disorders of red cell membrane. Br J Hematol 141:367–375

Arroyo M, Belytschko T (2002) An atomistic-based finite deformation membrane for single layer crystalline films. J Mech Phys Solids 50:1941–1977

Boey SK, Boal DH, Discher DE (1998) Simulations of the erythrocyte cytoskeleton at large deformation. I. microscopic models. Biophys J 75:1573–1583

Bratosin D, Tissier JP, Lapillonne H, Hermine O, de Villemeur TB, Cotoraci C, Montreuil J, Mignot C (2011) A cytometric study of the red blood cells in Gaucher disease reveals their abnormal shape that may be involved in increased erythrophagocytosis. Cytom B Clin Cytom 80B:28–37

Dao M, Lim CT, Suresh S (2003) Mechanics of the human red blood cell deformed by optical tweezers. J Mech Phys Solids 51:2259–2280

Dao M, Li J, Suresh S (2006) Molecularly based analysis of deformation of spectrin network and human erythrocyte. Mater Sci Eng C 26:1232–1244

Delaunaya J (2004) The hereditary stomatocytoses: genetic disorders of the red cell membrane permeability to monovalent cations. Semin Hematol 41:165–172

Discher DE, Boal DH, Boey SK (1998) Simulations of the erythrocyte cytoskeleton at large deformation. II. micropipette aspiration. Biophys J 75:1584–1597

Dolbow J, Belytschko T (1998) An introduction to programming the meshless Element free Galerkin method. Arch Comput Methods Eng 5:207–241

Fedosov DA, Caswell B, Karniadakis GE (2010) A multiscale red blood cell model with accurate mechanics, rheology, and dynamics. Biophys J 98:2215–2225

Guo X, Wang JB, Zhang HW (2006) Mechanical properties of single-walled carbon nanotubes based on higher order Cauchy–Born rule. Int J Solids Struct 43:1276–1290

Hansen JC, Skalak R, Chien S, Hoger A (1996) An elastic network model based on the structure of the red blood cell membrane skeleton. Biophys J 70:146–166

Hartmann D (2010) A multiscale model for red blood cell mechanics. Biomech Model Mech 9:1–17

Lancaster P, Salkauskas K (1981) Surfaces generated by moving least squares methods. Math Comput 37:141–158

Lenormand G, Hénon S, Richert A, Siméon J, Gallet F (2001) Direct measurement of the area expansion and shear moduli of the human red blood cell membrane skeleton. Biophys J 81:43–56

Liu S, Derick LH, Palek J (1987) Visualization of the hexagonal lattice in the erythrocyte membrane skeleton. J Cell Biol 104:527–536

Marko J, Siggia ED (1995) Stretching DNA. Macromolecules 28:8759–8770

Mills JP, Qie L, Dao M, Lim CT, Suresh S (2004) Nonlinear elastic and viscoelastic deformation of the human red blood cell with optical tweezers. Mech Chem Biosyst 1:169–180

Mukhopadhyay R, Lim GHW, Wortis M (2002) Echinocyte shapes: bending, stretching, and shear determine spicule shape and spacing. Biophys J 82:1756–1772

Sun Y, Liew KM (2008) Application of the higher-order Cauchy–Born rule in mesh-free continuum and multiscale simulation of carbon nanotubes. Int J Numer Methods Eng 75:1238–1258

Wang XY, Guo X (2012) Numerical simulation for finite deformation of single-walled carbon nanotubes at finite temperature using temperature-related higher order Cauchy–Born rule based quasi-continuum model. Comput Mater Sci 55:273–283

Wang XY, Guo X, Su Z (2014) A quasi-continuum model for human erythrocyte membrane based on the higher order Cauchy–Born rule. Comput Methods Appl Mech Eng 268:284–298

Yan JW, Liew KM, He LH (2013) Buckling and post-buckling of single-wall carbon nanocones upon bending. Compos Struct 106:793–798

Zhang P, Huang Y, Geubelle PH, Klein PA, Hwang KC (2002) The elastic modulus of single-walled carbon nanotubes: a continuum analysis incorporating interatomic potentials. Int J Solids Struct 39:3893–3906